arXiv:2610.28615v1 [cs.CV] 20 Oct 2026

KoalaGS: Complexity-Aware Continuous Level of Detail for Gaussian Splatting

Radu Beche[*]
TUCN

Raoul de Charette
Inria

https://rdbch.github.io/koalags

Abstract

Deploying a trained 3D Gaussian Splatting scene under shrinking compute budgets requires one primitive set to remain effective when rendered at smaller prefixes. In this continuous level of detail (LoD) setting, the challenge is to decide which Gaussians should retain capacity as the budget decreases. A pilot study on 3DGS-MCMC reconstructions shows that image complexity, computed from the input views before optimization, predicts where reconstruction error concentrates in image and 3D space. It also reveals that simple regions contain too many Gaussians and degrade as much as complex ones at lower budgets, despite being inherently cheaper to represent. Subsequently, in KoalaGS, during training we use this complexity prior to bias relocation toward poorly reconstructed areas while ensuring smooth degradation across LoDs. A primitive importance score then enables inference at low-capacity, while preserving the scene structure. Tested across three datasets, KoalaGS maintains competitive full-capacity quality while significantly improving quality across the budget spectrum, yielding smoother transitions across LoDs, and enabling faster progressive streaming.

1 Introduction

3D Gaussian Splatting [1] (3DGS) has made neural scene representations practical for novel view synthesis in real time. As the representation has matured, deployment under heterogeneous bandwidth and compute budgets has motivated a growing line of work on *continuous level of detail* (LoD) for 3DGS, where a single Gaussian set must remain useful when only a leading prefix of its primitives is retained [2, 3, 4]. The central problem in this setting is determining which primitives should retain capacity as the budget shrinks. Existing methods answer it implicitly, ranking primitives by opacity [2] or by learned importance scores [5]. A structural property of the representation suggests a complementary signal. A Gaussian does not contribute equally throughout a scene, as a single primitive may account for a broad region of nearly uniform appearance yet resolve only a fraction of a visually intricate one. We contend that this spatial variation in the value of capacity is what a continuous LoD policy should exploit, and we show that it can be anticipated from the input views alone.

We investigate this claim through a pilot study. Prior work already showed that global image complexity predicts reconstruction error in neural scene representations [6]; however, continuous LoD requires a localized signal that identifies not only which views are difficult, but where that difficulty lies within the scene. We therefore measure the correlation between local image complexity and reconstruction quality in the 2D image plane and, after multiview projection, on the Gaussian primitives. The correlation persists across DL3DV [7] and multiple complexity functionals in both domains, supporting complexity as a spatial prior for reconstruction difficulty that is available before optimization. We then examine how 3DGS-MCMC allocates capacity with respect to this structure. Gaussian density increases with complexity, approximately exponentially in regions of high

[*]Work done while visiting the Astra-Vision group at Inria, Paris.

Preprint.

complexity, yet even visually simple regions are represented by many low-opacity Gaussians. Under truncation according to opacity, quality degrades at comparable rates in simple and complex regions, showing that opacity alone does not expose the spatial redundancy required for robust continuous LoD. Together, these observations expose a mismatch between how 3DGS-MCMC allocates capacity at full budget and how effectively that allocation is preserved under truncation.

Our continuous LoD method for Gaussian Splatting addresses this mismatch. The key insight is that image complexity, which is predictive of reconstruction error, provides an inexpensive spatial prior for allocating capacity and selecting primitives as the budget shrinks. During optimization, a relocation rule biased by complexity steers primitives toward difficult regions, while at inference an importance score modulated by complexity preserves broad primitives in simple regions and relies primarily on opacity in complex ones. A residual variance objective further discourages an abrupt degradation as the budget shrinks. We evaluate the resulting representation along three complementary axes. Our method matches the best baselines at full capacity, while outperforming all continuous LoD baselines across the budget spectrum, even in extremely low budget ($< 1\%$). We show that this has great practical implication in streaming context, where our method improves drastically the time-to-quality performance.

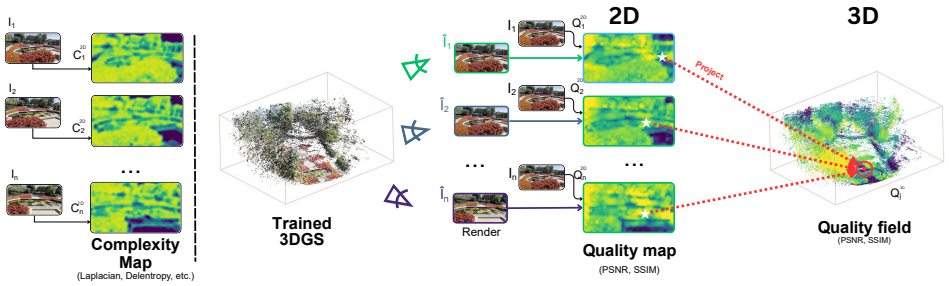
We summarize our contributions as follows:

- A pilot study on 140 DL3DV scenes showing image complexity predicts where reconstruction error concentrates, while capacity is allocated in a form that truncation cannot preserve.
- A continuous LoD method combining relocation biased by complexity during training, importance scoring modulated by complexity at inference, and a residual variance objective that discourages localized degradation across budgets.
- An evaluation of fixed budget quality, integrated spectrum quality, and transition variance, together with a streaming study showing a better time-to-quality tradeoff.

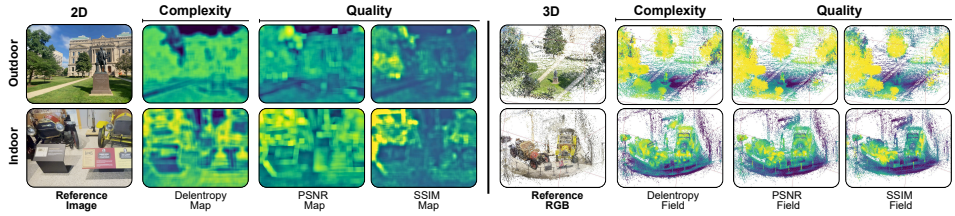
2 Related Work

Gaussian Splatting. 3D Gaussian Splatting transformed neural rendering by using an explicit set of anisotropic Gaussian primitives optimized for visibility-aware rasterization, enabling high-fidelity novel view synthesis at real-time frame rates [1]. A large body of literature focuses on making this representation more stable, efficient, and deployable. On the optimization side, [8] reformulates densification as probabilistic sampling over primitives, [9] introduces structured view-adaptive anchors, [10] incorporates radiance-field-informed optimization for robust high-speed rendering, while [11, 12, 13] reduce training cost or remove expensive densification mechanisms under constrained budgets. A complementary [14, 15] line compresses the trained representation itself, reducing memory footprint and rendering cost to make Gaussian scenes practical on resource-constrained devices. In parallel, other works [16, 17, 18] revisit the primitive parameterization, replacing or constraining 3DGS with 2D variants to improve geometric fidelity and compatibility with classical graphics pipelines. The flexibility of this representation also enables applications beyond static novel view synthesis, including dynamic scene modeling [19, 20], progressive and adaptive streaming [21, 22], mesh reconstruction [23], or higher-level scene understanding through language grounding, segmentation, and editing [24, 25]. Altogether, these works establish 3DGS as a general explicit scene representation. Our work employs 3DGS for deployment under heterogeneous primitive budgets, exposing image complexity as a spatial prior over both densification and ranking.

Level of Detail in Gaussian Splatting. A growing body of work ports classical Level of Detail [26] into the splatting pipeline. A first category imposes *explicit* hierarchies over the primitive set and exposes a small number of discrete operating points [27, 28, 29], with spatial divide and conquer variants scaling to kilometer sized captures [30, 31, 32]. A second category approximates multi budget behavior through compression and importance pruning at varying targets [12, 15], where each operating point is optimized independently and a new model must be retrained for every budget. A third category pursues *continuous* LoD over a single primitive set: [3, 4] learn per Gaussian distance dependent opacity decay, while FlexGS [5] learns a differentiable budget conditioned selector that achieves strong quality at targeted budgets but requires a fresh forward pass at every LoD change, precluding progressive streaming. Closer to our setting, Matryoshka-GS [2] introduces a nested prefix renderable ordering trained via stochastic budget sampling, so that any leading slice yields a coherent reconstruction. Our work belongs to this last category but departs from prior approaches in how the ordering is determined: we introduce image complexity as a scene side spatial prior over



(a) Analysis methodology



(b) Qualitative examples

Figure 1: **Analysis methodology.** (a) We measure the spatial correlation between the complexity map of the input image (left), and the quality map (center), obtained after 3DGS-MCMC optimization. We then project and aggregate these 2D fields onto the Gaussian particles to obtain complexity/quality fields in 3D (right). (b) Complexity and quality inversely correlate both in the 2D image plane and in the 3D object space. *Note that for easier visualization, we inverted colors of all complexity maps.*

both densification and ranking, and train for spatial uniformity of the residual between full capacity and prefix renders.

3 Pilot Study

This section studies image complexity as a predictor of 3DGS reconstruction quality, computed from the input views before any optimization. The outcomes will shape our method, which must decide where to spend capacity at the moment when reconstruction error, the signal that would otherwise guide it, is not yet available. The intuition is that deploying under a primitive budget is a spatial decision. As primitives are withdrawn, some regions tolerate the loss while others do not, so the capacity that remains should sit where reconstruction error concentrates. Image complexity addresses this, since prior work [6] shows that it predicts reconstruction error and is read from the input images before optimization rather than recovered after training. What that work leaves open is whether the signal is spatial, since an image level score ranks views by difficulty but not where the error lies within them. We therefore investigate two questions: **(i)** Does complexity localize reconstruction error in space, across the image plane and the 3D world? **(ii)** Are trained models already allocating capacity where complexity predicts it should? For experimental details we refer to Sec. B.1.

Does complexity spatially correlate with reconstruction error? To address this, we first analyze the spatial distribution of complexity with respect to the reconstruction quality metrics, seeking to study how the two correlate both in the 2D image space and 3D space. The overall methodology is shown in Fig. 1a. Specifically, we define two spatially indexed fields over image patches. Let $\hat{I}_i = \mathcal{R}_\theta(\Pi_i)$ denotes the rendering of a trained 3DGS-MCMC model under camera Π_i, and let $R(u) \subset \Omega$ be a receptive field centered at pixel u. For 2D, we define the quality map and complexity map as:

$$Q_i^{\mathrm{2D}}(u) = \frac{1}{|R(u)|} \sum_{v \in R(u)} q\Big(I_i(v), \hat{I}_i(v)\Big), \quad C_i^{\mathrm{2D}}(u) = H\Big(I_i\big|_{R(u)}\Big), \tag{1}$$

where H is a local complexity functional and q is a local quality measure, with higher values indicating better reconstruction. To obtain their 3D counterparts, we project all quality maps Q_i^{2D} and complexity maps C_i^{2D} onto the Gaussian particles under multiview aggregation, obtaining a single quality field Q^{3D} and complexity field C^{3D} per scene. To do so, we define the contributing view set

Domain	Complexity	Pearson ρ		Spearman r_s		Avg. Rank
		PSNR	SSIM	PSNR	SSIM	
2D	Shannon	-0.605	-0.259	-0.590	-0.346	3
	Laplacian	-0.546	-0.207	$\mathbf{-0.649}$	-0.365	2
	Delentropy	$\mathbf{-0.647}$	$\mathbf{-0.379}$	-0.638	$\mathbf{-0.498}$	**1**
	Average	-0.599	-0.282	-0.626	-0.403	–
3D	Shannon	-0.588	-0.557	-0.170	-0.165	3
	Laplacian	-0.655	$\mathbf{-0.688}$	-0.224	-0.267	2
	Delentropy	$\mathbf{-0.678}$	-0.646	$\mathbf{-0.384}$	$\mathbf{-0.388}$	**1**
	Average	-0.640	-0.630	-0.259	-0.273	–

Table 1: **Correlation between local complexity and reconstruction quality.** On DL3DV, across 140 scenes, complexity is negatively correlated with PSNR and SSIM in both the image plane and object space, indicating that more complex regions tend to reconstruct worse. Delentropy gives the strongest average rank. Best correlations are shown in bold.

as $\mathcal{I}(\mathbf{x}) = \{\, i : \pi_i(\mathbf{x}) \in \Omega \text{ and } \mathbf{x} \text{ visible in view } i \,\}$, the views in which $\mathbf{x}$ projects inside the image domain and is not occluded, so that each point aggregates evidence only from views that observe it. Considering all 3D Gaussian positions $\mathbf{x}$, we then define the 3D fields via direct projection such that:

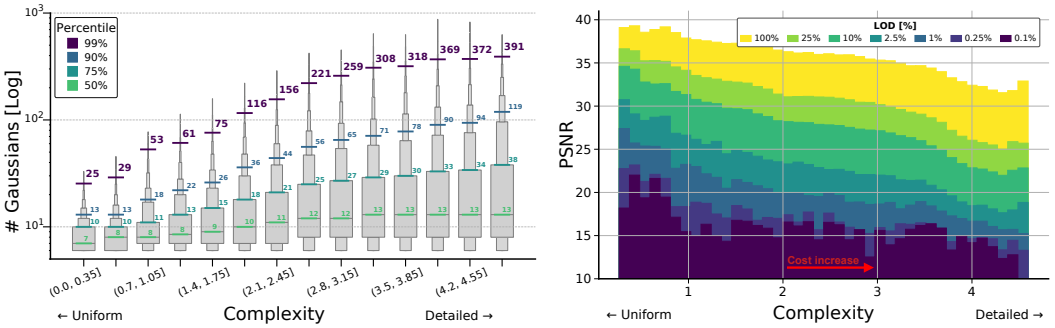
$$Q^{\text{3D}}(\mathbf{x}) = \frac{1}{|\mathcal{I}|} \sum_{i \in \mathcal{I}} Q_i^{\text{2D}}(\pi_i(\mathbf{x})) \quad \text{and} \quad C^{\text{3D}}(\mathbf{x}) = \frac{1}{|\mathcal{I}|} \sum_{i \in \mathcal{I}} C_i^{\text{2D}}(\pi_i(\mathbf{x}))\,. \tag{2}$$

In Fig. 1b we report qualitative visuals on bounded and unbounded scenes. They highlight that regardless of the scene type, the complexity and quality fields generally correlate visually. This is very much noticeable on the outdoor pathway which are low complexity regions that also exhibit a low reconstruction error (high quality score).

We further measure quantitatively the statistical correlations of quality and complexity using the Pearson correlation ρ which denotes the linear association, and the Spearman rank correlation r_s. For 2D, correlation is observed on paired observations $\{(C_i^{\text{2D}}(u),\, Q_i^{\text{2D}}(u))\}$ over all patches and views, while for 3D metrics we evaluate $\{C^{\text{3D}}(\mathbf{x}),\, Q^{\text{3D}}(\mathbf{x})\}$ over all Gaussian locations. Regardless of the measure used, results in Tab. 1 show consistently high correlation, with large negative values indicating that highly complex regions consistently lead to low reconstruction quality. *In the 2D image plane*, all three measures exhibit a consistent negative association with patch level quality across scenes and views. The effect is stronger under PSNR ($|\rho|, |r_s|$ in the range 0.55–0.65) than SSIM (0.21–0.50). Among the functionals, *delentropy* exhibits the strongest correlation, and we adopt it in our method. *In the 3D object space*, the picture refines rather than uniformly attenuates. Compared to the 2D metrics, aggregation reduces view dependent appearance noise and recovers a clearer linear relationship (*i.e.*, stronger Pearson correlation), whereas the rank correlations lower substantially ($|r_s| \approx 0.17$–0.39). The interpretation is that multi view averaging preserves the gross magnitude relationship between complexity and quality but compresses the tails of both fields, degrading the fine ordering even where the linear association strengthens. This empirical evidence supports that image complexity provides a spatial cue about *where* reconstruction errors emerge, both within a view and within a scene. To further establish complexity as a usable spatial prior over reconstruction difficulty, we study how Gaussians are allocated with respect to complexity.

Does complexity correlate with Gaussian density? Since complexity correlates with the reconstruction error, it is reasonable to expect that the optimal 'per region number of Gaussians' is already achieved. Indeed, density control mechanism (pruning, cloning, relocation) for 3DGS are designed to increase Gaussian density where reconstruction error is higher. To relate density to complexity at the scene level, we voxelize each scene at a fixed edge length of 0.1 in normalized scene coordinates and, within every voxel, record the mean complexity, the mean reconstruction quality, and the number of Gaussians whose centers fall inside. The fixed scale is well defined because DL3DV test scenes are released in a comparable spatial scale across scenes.

Reporting the resulting Gaussian counts across complexity intervals in Fig. 2a, we observe that more complex voxels hold more Gaussians, generally following an exponential trend. At the 90th percentile, the ratio between the least and most complex voxels (13 vs. 119 Gaussians per voxel) is surprising, since the simplest voxels typically depict uniform color and are expected to be reconstructed with only a few Gaussians. We therefore question whether the Gaussian budget is correctly utilized across regions of varying complexity.



(a) Number of Gaussians (log-scale) per complexity

(b) Quality (PSNR ↑) for varying LOD

Figure 2: **Relation between complexity and Gaussian density.** (a) Each bin counts the Gaussians inside a voxel of that complexity aggregated across DL3DV scenes. On the y-axis, the straight rise of the percentiles indicates an exponential growth (note y-axis is log-scaled). (b) Considering an indoor scene reconstructed with 3DGS-MCMC, we lower capacity by dropping primitives in order of opacity, plotting the average PSNR reached at each complexity for every budget. We observe that the simplest regions lose almost as much quality as the most complex ones, so even flat surfaces are broken into multiple low opacity Gaussians.

To verify this, we implement a naive LoD strategy which preserves only the top X% of Gaussians by opacity. Varying LoD from 100% (*i.e.*, full capacity) to 0.1%, in Fig. 2b we report the PSNR across complexity for a representative scene. While overall PSNR decreases expectedly with complexity and LoD, the study reveals another intriguing characteristic. Decreasing LoD from 100% to 0.1% lowers quality nearly equally in complex regions ($\approx -62\%$ PSNR) and in simple regions ($\approx -58\%$ PSNR). This indicates that, even in the simplest regions, 3DGS-MCMC favors decomposing visual signals into multiple *lower-opacity* Gaussians. Moreover, PSNR fluctuations across complexity reveal uneven Gaussian opacities. Altogether, these observations show that while 3DGS-MCMC reconstructions are denser in complex regions, Gaussians remain suboptimally distributed across complexities. We further analyze how Gaussians are allocated and retained across complexity levels in Sec. D.4.

4 Method

We consider the continuous level of detail setting for 3DGS. Given a posed training set $\mathcal{D} = \{(I_i, \Pi_i)\}_{i=1}^{M}$, the goal is to learn a single Gaussian representation $\mathcal{G} = \{g_j\}_{j=1}^{N}$ that can be rendered under a variable primitive budget $\tau \in (0, 1]$, such that

$\mathcal{G}_\tau \subseteq \mathcal{G}$ with $|\mathcal{G}_\tau| = \lceil \tau N \rceil$. At every budgeted representation, our aim is that $\mathcal{G}_\tau$ remains spatially coherent and degrades gracefully as τ decreases. Following our pilot study (Sec. 3) which demonstrates that image complexity is a surrogate of the reconstruction error, our aim is to benefit from the image complexity signal, readily accessible at training time. Specifically, we apply two simple modifications to the optimization process of state-of-the-art 3DGS-MCMC [8]. First, we utilize complexity to foster (re)allocation of the Gaussians in regions with higher complexity (Sec. 4.1). Second, we introduce a content-aware importance score that retains simple regions at low budgets (Sec. 4.2). We complement them with a residual variance objective that encourages stable reconstruction error across space and LoDs. Experiments show that our simple modification boost performance and efficiency. The proposed LoD is global and view independent, rather than conditioned on camera distance or screen resolution. The implications are further discussed in Sec. B.2.

Preliminaries. A 3DGS representation encodes a scene as a set of Gaussian primitives, where each Gaussian $g_j = (\mu_j, \alpha_j, \Sigma_j, \mathbf{c}_j)$ is parameterized by its position μ_j, opacity α_j, covariance Σ_j, and color coefficients $\mathbf{c}_j$. To expose complexity to the optimization process, we augment each primitive with a scalar variable C_j, which stores the local image complexity associated with the current Gaussian. This relates to the complexity field in Eq. 2, but differs from the post-hoc analysis in our pilot study since, during training, Gaussian positions and supports change, and therefore their complexity values must be updated online.

To address this, after each full-capacity training render of a view Π_i, we project the means of the contributing Gaussians into the image plane, and update each particle's complexity via an exponential moving average, using the complexity map $C_i^{\text{2D}}(u)$ from Eq. 1, computed with delentropy. So that:

$$C_j \;\leftarrow\; (1-\eta)\, C_j \;+\; \eta\, C_i^{\text{2D}}\big(\pi_i(\mu_j)\big), \qquad \eta \in (0,1]. \tag{3}$$

Only particles whose centers project in the current view's frustum are updated. Over the course of training each particle's C_j converges to the multi-view average similar to those in Eq. (2). At last, S_j is the importance score of a particle used for prefix sorting computed using the scoring function $S(\cdot)$.

4.1 Complexity-aware Adaptive density control

In practice, 3DGS variants rely on opacity as a proxy for this error signal: during optimization new primitives are concentrated where opacity has accumulated, and regions the optimizer has not yet resolved remain under-served precisely because they have not been resolved. In 3DGS-MCMC [8], the probability p to relocate at the coordinate of μ_j writes: $p(g_j) = \alpha_j$. Given that complexity is a surrogate of reconstruction errors (*cf.*, Tab. 1), we simply bias this sampling weight towards more complex regions. We therefore sample relocation destinations with:

$$p(g_j) = \alpha_j \cdot \exp\big(\tilde{C}_j\big)\,, \tag{4}$$

where $\tilde{C}_j \in [0,1]$ is the min-max normalized C_j. Note that we utilize $\exp(\cdot)$ to mimic the exponential growing behavior of particles count with complexity, as in the 90th percentile in Fig. 2a. Importantly, the multiplicative form keeps opacity in the loop since a primitive that has earned its keep should not be evicted for exploring other regions. To prevent collapse onto fixed complex regions, we apply *complexity dropout*, setting $\tilde{C}_j = 0$ with probability $\delta = 0.2$ (ablated in Sec. D.2) and thus scoring that fraction of relocation candidates by opacity alone (δ=0: none; δ=1: all).

4.2 Complexity-aware Level of Details

As mentioned in Sec. 3, under a limited budget (*i.e.*, $\tau < 1$), only Gaussians with the highest importance score $S(\cdot)$ are preserved. In the literature, this typically resolves to using opacity [2], *i.e.*, $S(g_j) = \alpha_j$. As shown in Fig. 2b, this degrades low-complexity regions as much as complex ones, although they should be the cheapest to retain, because opacity captures learned contribution but not the total spatial footprint over which a primitive contributes. We therefore rank primitives by combining three complementary signals: opacity, scale, and complexity:

$$S(g_j) = \alpha_j + \lambda \cdot \frac{s(g_j)}{\exp\big(\tilde{C}_j(\mu_j)\big)}, \tag{5}$$

where $s(g_j)$ is the max-normalized scale of g_j and $\lambda = 2$ is a fixed scalar weight. The three components play distinct, complementary roles. Opacity captures the importance learned through the photometric objective, allowing a small high-opacity Gaussian to outrank a moderate-opacity one that covers a broader region. Scale supplies this missing spatial footprint, while complexity controls where it should influence the score. In high-complexity regions, $\exp(C)$ attenuates the scale term, avoiding preference for large, potentially blurring primitives and reducing the score toward opacity, which is most reliable where optimization pressure is concentrated. In low-complexity regions, where preserving broad spatial support matters more, the second term reduces to $\lambda \cdot s$ as $\exp(C) \to 1$, restoring weight to large primitives that efficiently cover simple areas despite their moderate opacity.

We note that LoD-awareness requires the optimizer to vary LoD (*i.e.*, τ) during training. However, the scoring alone does not guarantee that the resulting render degrades uniformly since the optimization support varies with τ. Namely, at full-capacity ($\tau = 1$) the optimizer has access to all primitives to fit the image, while at lower LODs ($\tau < 1$) the optimizer only accesses the surviving primitives (according to Eq. 5) and may push the latter away from their full-capacity solution. To keep the resulting deviation spatially uniform, we consider the residual of the reconstruction error between full-capacity render and lower LODs render, and minimize it's variance.

Formally, at each step we compute the residual of the reconstruction error $\mathcal{E}(\cdot)$ at τ and at full-capacity: $\Delta_i = \mathcal{E}(I_i^{\text{full}}) - \mathcal{E}(I_i^{\tau})$, and minimize its spatial variance:

$$\mathcal{L}_{\text{var}} \;=\; \text{Var}_{u\in\Omega}\big(\Delta_i(u)\big). \tag{6}$$

	Method	#GS [k]	100% Capacity			10% Capacity			1% Capacity			0.1% Capacity		
			PSNR ↑	SSIM ↑	LPIPS ↓	PSNR ↑	SSIM ↑	LPIPS ↓	PSNR ↑	SSIM ↑	LPIPS ↓	PSNR ↑	SSIM ↑	LPIPS ↓
DB	OctreeGS [27]	1,457	30.23	0.908	0.254	-	-	-	-	-	-	-	-	-
	FlexGS [5]	2,547	29.29	0.898	0.320	29.27	0.897	0.349	24.68	0.824	0.472	-	-	-
	3DGS MCMC [8]	2,950	29.70	0.907	**0.236**	24.36	0.792	0.362	16.81	0.656	0.520	12.67	0.601	0.599
	LightGaussian [15]	2,950	29.73	0.907	0.240	26.21	0.849	0.333	19.59	0.742	0.482	15.26	0.675	0.546
	MGS [2]	2,950	29.29	0.905	0.247	28.61	0.888	**0.282**	23.28	**0.800**	**0.416**	16.58	0.692	0.531
	Ours	2,950	**29.92**	**0.911**	0.240	**29.05**	**0.890**	**0.282**	**23.40**	0.798	0.419	**17.81**	**0.720**	**0.522**
MipNerf	OctreeGS [27]	2,991	29.16	0.876	0.174	-	-	-	-	-	-	-	-	-
	FlexGS [5]	3,012	29.06	0.872	0.217	27.58	0.835	0.293	23.39	0.663	0.494	-	-	-
	3DGS MCMC [8]	3,092	29.80	0.893	**0.146**	20.58	0.647	0.352	14.14	0.383	0.586	11.06	0.267	0.667
	LightGaussian [15]	3,092	**29.89**	**0.897**	0.147	21.06	0.669	0.359	15.81	0.475	0.558	13.01	0.377	0.636
	MGS [2]	3,092	29.55	0.890	0.151	26.97	0.797	0.280	20.17	0.544	0.521	14.49	0.393	0.620
	Ours	3,092	29.80	0.893	0.150	**27.82**	**0.822**	**0.258**	**21.14**	**0.566**	**0.510**	**16.04**	**0.459**	**0.611**
TandT	OctreeGS [27]	2,080	24.45	0.860	0.158	-	-	-	-	-	-	-	-	-
	FlexGS [5]	1,979	23.78	0.847	0.204	23.06	0.807	0.278	19.49	0.642	0.478	-	-	-
	3DGS MCMC [8]	1,850	24.43	0.866	**0.143**	18.52	0.670	0.356	11.96	0.404	0.589	8.92	0.306	0.680
	LightGaussian [15]	1,850	24.46	0.863	0.146	19.17	0.680	0.347	13.21	0.453	0.596	9.52	0.351	0.686
	MGS [2]	1,850	24.40	0.864	0.150	22.16	0.755	0.309	16.66	0.536	0.526	**12.10**	0.410	**0.639**
	Ours	1,850	**24.65**	**0.868**	0.150	**22.97**	**0.785**	**0.277**	**17.38**	**0.551**	**0.519**	11.56	**0.413**	0.660

Table 2: **Performance at log-spaced LoD targets.** Metrics at 100%, 10%, 1%, and 0.1% budgets across three datasets. Among full-LoD methods, ours performs on par at full capacity and generally better at lower budgets. For partial-LoD methods, dashes (-) denote unreachable operating points.

Training objectives. We use the L1+D-SSIM loss of 3DGS-MCMC on the full ($\tau = 1$) and budgeted ($\tau < 1$) renders, add $\lambda_{\text{var}}\mathcal{L}_{\text{var}}$, and average them. Training details are given in Sec. B.2.

5 Experimental Results

We evaluate our method on three datasets [33, 34, 35] and compare its performance against five baselines [2, 5, 15, 27, 8]. Since performance of LoD-aware 3DGS may vary across LoD, it is not possible to characterize its performance by a single metric. We therefore assess our method along three complementary axes: *quality* at predefined LoD targets (Sec. 5.1), *spectrum quality* as the per-metric area under the curve over the full LoD sweep (Sec. 5.2), and *intra- and inter-LOD transition variance* (Sec. 5.3), which together capture whether quality is high, whether it is sustained across the spectrum, and whether it degrades gracefully rather than abruptly. We further conduct an ablation in Sec. 5.4 to isolate the contribution of each component of our method. We refer the reader to Sec. C for the experimental setup description and Sec. D for additional experiments. In all tables, best results are in **bold** and second best are underlined.

5.1 Quality at Predefined LOD Targets

We first ask whether our method delivers high quality at the operating points a user is most likely to deploy, therefore evaluating at four log-spaced budgets chosen to probe each decade of the spectrum: 100% reflects full-capacity quality, 10% a moderate compression regime relevant to deployment, 1% an aggressive reduction where ranking quality dominates and an extreme 0.1%, [typically used when initialising a streaming]. Quantitative results are reported in Tab. 2, while separating partial-LoD methods (OctreeGS, FlexGS) as they can only be evaluated at some intervals. Qualitatives are presented in Fig. 3, and curves are visualized in Fig. 4. A consistent picture emerges across datasets. *At full capacity*, all methods are competitive (Fig. 3, top row), with our method performing generally on par with the strongest baseline on every dataset and confirming that content-aware modifications introduce no penalty at peak fidelity. *As the budget shrinks*, the field separates sharply. 3DGS MCMC degrades rapidly and has already collapsed by the 1% threshold, confirming that opacity-based ranking alone cannot sustain quality under reduction. LightGaussian retains more quality than opacity-based pruning in most cases, but falls behind both MGS and ours at every reduced budget across all three datasets. OctreeGS cannot operate below its native discrete levels and it remains competitive only on the indoor Deep Blending scenes and falls behind on outdoor scenes. FlexGS, which is not prefix renderable, trades this property for higher quality near the specific operating points it was optimised for, but degrades unpredictably between them. MGS, our closest competitor, follows the same trend as our method but consistently lags behind it. Altogether, content-aware ranking yields a more robust quality versus quantity trade-off than any single-family representative, both quantitatively and visually. We report the rendering speeds in Sec. D.3 and further investigate how our importance score and densification behave jointly in Sec. D.4.

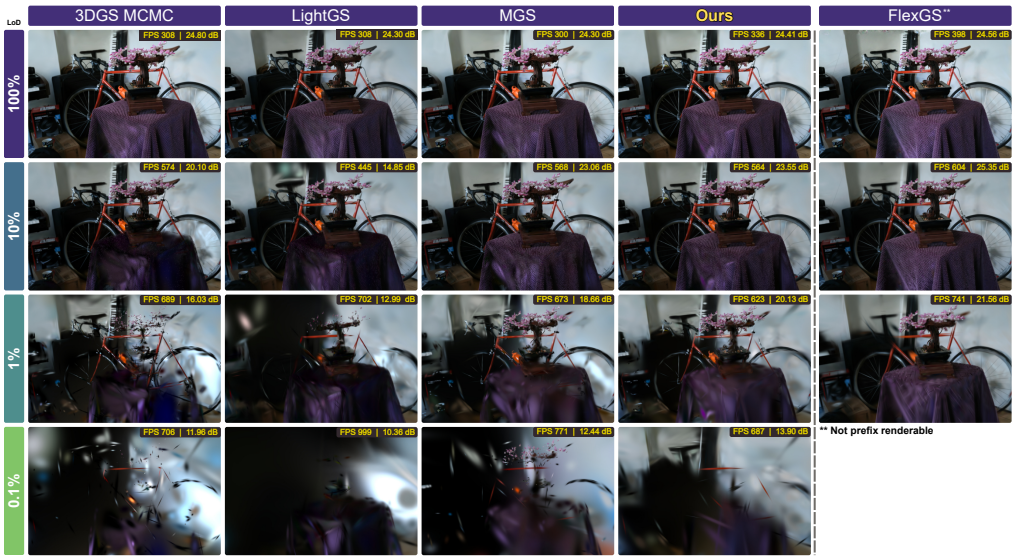


Figure 3: **Qualitative comparison across the LoD spectrum.** Methods perform similarly at full capacity but diverge sharply at lower budgets. Ours better preserves scene coverage at low budgets and remains competitive with FlexGS while enabling prefix rendering.

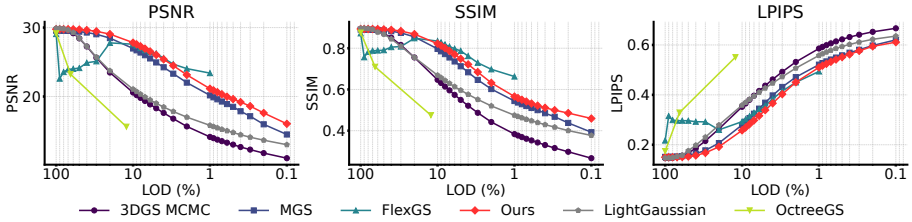


Figure 4: **Quality metrics across the LoD spectrum.** Our method matches full-capacity baselines and degrades more gracefully as budgets shrink. Below 10%, 3DGS MCMC collapses and LightGaussian improves little. OctreeGS has limited discrete LoDs, FlexGS fluctuates between trained budgets, and MGS follows ours but with lower quality throughout. Results are on MipNerf.

5.2 Quality Across the LoD Spectrum

The previous section leaves open how quality evolves *across the full LoD spectrum*. To address this, we sample 28 operating points in $[0.1\%, 100\%]$, ten linearly spaced per interval ($[0.1\%, 1\%]$, $[1\%, 10\%]$, $[10\%, 100\%]$) with shared endpoints, and integrate per-metric curves with the trapezoidal rule to compute interval-wise area-under-the-curve (AUC) score, rescaled per interval for direct comparison. Since discrete methods cannot operate across the full spectrum, we focus on prefix-renderable continuous LoD methods. From results in Tab. 3, our method consistently achieves the highest AUC. Since the total AUC is dominated by high budgets where all methods cluster, the sub-interval breakdown is more informative. 3DGS MCMC collapses below 10% capacity, yielding the lowest sub-interval AUC across datasets and confirming that opacity-based ranking alone fails as the budget shrinks. LightGaussian improves PSNR and generally SSIM over opacity-based pruning, but remains behind MGS and ours across all metrics in the two lower-budget intervals. Our largest gain over MGS occurs precisely in the low-budget $[0.1\%, 1\%]$ regime where ranking quality dominates. FlexGS performs better at $[1\%, 10\%]$, but it does not allow full LoD coverage. Besides, FlexGS is outperformed by ours in other intervals, which directly results from its design as it trained for specific operating points at the cost of global consistency, producing the irregular degradation curves visible in Fig. 4. Overall, these results indicate that our method offers the most balanced quality versus quantity trade-off across the LoD spectrum.

5.3 LoD Transition Variance

We further assess whether our method enables fine-grained reconstruction control with smooth quality degradation. Indeed, the above mentioned metrics do not capture spatial or LoD consistency: a

	Method	Total [0.1%, 100%]			[0.1%, 1%] (×100)			[1%, 10%] (×10)			[10%, 100%]		
		AUC PSNR ↑	AUC SSIM ↑	AUC LPIPS ↓	AUC PSNR ↑	AUC SSIM ↑	AUC LPIPS ↓	AUC PSNR ↑	AUC SSIM ↑	AUC LPIPS ↓	AUC PSNR ↑	AUC SSIM ↑	AUC LPIPS ↓
DB	FlexGS [5]	27.47	0.867	0.363	-	-	-	25.28	0.788	0.350	24.94	0.788	0.328
	3DGS MCMC [8]	27.96	0.870	0.274	13.69	0.573	0.497	19.49	0.664	0.378	25.87	0.798	0.231
	LightGaussian [15]	28.61	0.888	0.268	16.29	0.650	0.457	21.44	0.730	0.347	26.31	0.809	0.229
	MGS [2]	28.95	0.897	0.259	18.81	0.685	0.414	24.62	**0.778**	0.289	26.30	0.813	0.226
	Ours	**29.51**	**0.902**	**0.254**	**19.19**	**0.690**	**0.413**	**24.86**	**0.778**	**0.288**	**26.83**	**0.817**	**0.221**
MipNerf	FlexGS [5]	24.77	0.792	0.293	-	-	-	23.36	0.698	0.328	22.43	0.722	0.260
	3DGS MCMC [8]	26.58	0.814	0.213	11.69	0.307	0.559	16.39	0.493	0.395	24.83	0.762	0.168
	LightGaussian [15]	26.78	0.820	0.218	14.75	0.438	0.592	19.03	0.596	0.430	24.93	0.762	0.174
	MGS [2]	28.65	0.858	0.192	16.45	0.445	0.503	22.27	0.636	0.334	26.25	0.790	0.153
	Ours	**29.09**	**0.867**	**0.184**	**17.55**	**0.471**	**0.496**	**23.20**	**0.665**	**0.311**	**26.59**	**0.795**	**0.147**
Tand T	FlexGS [5]	21.89	0.788	0.262	-	-	-	19.82	0.679	0.308	19.91	0.720	0.231
	3DGS MCMC [8]	22.50	0.801	0.212	9.74	0.331	0.561	14.42	0.510	0.406	20.96	0.747	0.166
	LightGaussian [15]	22.74	0.802	0.211	10.66	0.376	0.570	15.30	0.534	0.394	21.11	0.745	0.166
	MGS [2]	23.59	0.827	0.201	13.67	0.442	0.519	18.28	0.609	0.353	21.62	0.762	0.160
	Ours	**24.02**	**0.839**	**0.189**	**13.83**	**0.447**	**0.517**	**19.05**	**0.637**	**0.327**	**21.98**	**0.771**	**0.151**

Table 3: **Area Under the Curve (AUC) across Capacity Intervals.** For all intervals, our method outperforms all other prefix-renderable continuous LoD methods, exhibiting large gaps in smaller intervals $[0.1\%, 1\%]$. Intervals are scaled for direct comparison.

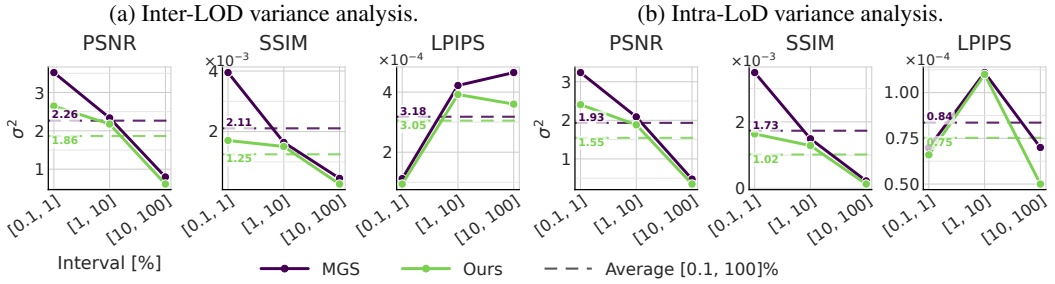


Figure 5: **Variance analysis across LoD.** For both MGS and ours, we report the inter and intra LoD variances on MipNerf(*lower is better*). Our method consistently outperforms MGS.

method that concentrates errors in localized regions may rank highly while exhibiting abrupt changes across LoDs. To analyze this, we compute per-pixel error maps following Sec. 3 and derive two complementary variance measures. *Inter-LoD variance* captures transitions across levels: for each patch, we take differences between error maps at consecutive LoDs, compute the variance of these residuals, and average over all patches. Low values indicate smooth rather than abrupt degradation. *Intra-LoD variance* measures spatial uniformity within a level: we compute the variance of each error map across patches and average over LoDs. Low values indicate that errors are evenly distributed rather than concentrated in localized regions. Neither measure is meaningful in isolation, as uniformly poor renderings can also yield low variance. We therefore use them as a *complement* to the absolute quality metrics reported above. Further details are provided in Sec. E. Results on MipNerf against MGS are reported in Fig. 5. Across all intervals and metrics, our method exhibits lower inter-LoD variance than MGS, with the gap being most pronounced in the $[0.1\%, 1\%]$ regime where budget pressure is highest and abrupt transitions are most likely to occur. A consistent reduction is also observed in intra-LoD variance, indicating that our content-aware ranking not only smooths transitions across levels but also distributes error more uniformly within each level. Taken together with the absolute and AUC results, these findings confirm that complexity-aware importance scoring yields a representation that degrades both more gracefully and more uniformly across the full LoD spectrum.

5.4 Ablation Study

To isolate the individual and combined contributions of our three additions, we evaluate all combinations of content-aware densification (Dens.), content-aware importance scoring (Score), and the spatial variance loss (Var.). We report both full-capacity quality (100%) and the per-metric AUC over the LoD spectrum $[0.1\%, 100\%]$ in Tab. 4. Each component alone improves upon the baseline across all AUC metrics, except Var., which matches the baseline in AUC SSIM. Densification provides the largest standalone improvement at full capacity, while importance scoring yields the largest standalone AUC gains. Among the two-component configurations, Dens.+Score performs best

	Components			AUC [0.1%, 100%]			100% Capacity		
	Dens.	Score	Var.	PSNR ↑	SSIM ↑	LPIPS ↓	PSNR ↑	SSIM ↑	LPIPS ↓
None	✗	✗	✗	28.74	0.855	0.196	29.55	0.863	0.164
Single	✓	✗	✗	28.81	0.859	0.190	29.79	0.889	0.151
	✗	✓	✗	28.94	0.861	0.188	29.62	0.882	0.159
	✗	✗	✓	28.79	0.855	0.190	29.59	0.870	0.160
Pair	✓	✓	✗	28.99	0.862	0.187	29.75	0.885	0.154
	✓	✗	✓	28.75	0.850	0.197	29.70	0.877	0.159
	✗	✓	✓	28.95	0.860	0.189	29.71	0.880	0.155
All	✓	✓	✓	**29.09**	**0.867**	**0.184**	**29.80**	**0.893**	**0.150**

Table 4: **Full ablation.** All combinations of complexity-aware densification (Dens.), importance scoring (Score), and the spatial variance loss (Var.) on MipNerf.

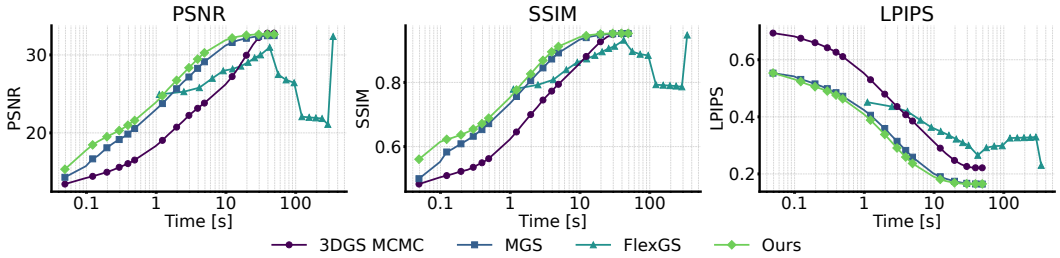


Figure 6: **Time to quality in streaming.** Rendering quality of Bonsai [34], over a 50 Mbps link. Prefix methods send each primitive once, so every arrival refines the model, and ours reaches every quality level first. FlexGS resends the full set for each budget, so time is delayed and quality oscillates.

across both full-capacity and AUC metrics. However, adding Var. to either component alone does not consistently improve performance, suggesting that its benefit depends on the accompanying allocation and ranking mechanisms. The complete configuration achieves the best full-capacity quality and integrated quality across all three metrics, supporting the combined use of the three components. A more detailed breakdown of the ablation results at individual LoD budgets is provided in Sec. D.5.

5.5 Application: time-to-quality in streaming

Our ranking naturally enables progressive streaming, where remote clients render the primitives as they arrive. Prior 3DGS streaming systems use a few discrete quality layers [21] without characterizing how quality evolves throughout streaming. We therefore measure *time to quality*: the time to reach a target rendering fidelity at fixed bandwidth. We simulate 50 Mbps bandwidth (representative of 5G network), and send each primitive as raw fp32 attributes (236 bytes). We compare against MGS [2] and 3DGS MCMC [8], which stream incrementally like ours, and FlexGS [5], which must restream the full set at every budget. On the Bonsai scene of MipNerf [34] (Fig. 6), the prefix methods receive the full model in 49.1 s, while FlexGS needs 344 s, a 7.0× overhead caused by restreaming. Our method reaches 25 dB after 1.47 s, compared to 1.96 s for MGS and 9.82 s for 3DGS MCMC, and 28 dB after 2.95 s, compared to 3.93 s and 14.73 s, respectively. FlexGS is also non monotone in time, dropping to about 22 dB in the mid budgets before recovering at full capacity. Because our importance score (Eq. 5) sends large primitives in simple regions first, the client sees a complete, coarse scene within the first timestamps.

6 Conclusion

We studied how to allocate Gaussian primitives as rendering budgets shrink in continuous LoD splatting. Our pilot study showed that image complexity, accessible before any optimization, predicts spatial reconstruction error in 2D and 3D, yet trained models fail to allocate capacity accordingly in a form that a shrinking budget preserves. Building on these observations, we design a method allocating primitives based on complexity which determines their survival at inference, using a variance objective to maintain uniform error across scales. Evaluated on three datasets, our approach matches the strongest baselines at full capacity, while achieving the highest integrated quality across budgets, and degrades more gracefully, with the largest gains below 1% capacity and faster time-to-quality in streaming.

Acknowledgments and Disclosure of Funding

This work was supported by the "Romanian Hub for Artificial Intelligence-HRIA", Smart Growth, Digitization and Financial Instruments Program, MySMIS no. 351416 and by the Astra Team, Inria. This work was granted access to the HPC resources of IDRIS under the allocation 2025-AD011017283 made by GENCI on the Jean-Zay Cluster. The authors would like to thank Sergiu Nedevschi and Fawzi Nashashibi for making this collaboration possible.

References

[1] Bernhard Kerbl, Georgios Kopanas, Thomas Leimkühler, and George Drettakis. 3d gaussian splatting for real-time radiance field rendering. *ACM Transactions on Graphics*, July 2023.

[2] Zhilin Guo, Boqiao Zhang, Hakan Aktas, Kyle Fogarty, Jeffrey Hu, Nursena Koprucu Aslan, Wenzhao Li, Canberk Baykal, Albert Miao, Josef Bengtson, et al. Matryoshka gaussian splatting. *arXiv preprint arXiv:2603.19234*, 2026.

[3] Zhigang Cheng, Mingchao Sun, Yu Liu, Zengye Ge, Luyang Tang, Mu Xu, Yangyan Li, and Peng Pan. CLod-GS: Continuous level-of-detail via 3d gaussian splatting. In *The Fourteenth International Conference on Learning Representations*, 2026.

[4] A Božič. Learning fast 3d gaussian splatting rendering using continuous level of detail. In *Computer Graphics Forum*, 2025.

[5] Hengyu Liu, Yuehao Wang, Chenxin Li, Ruisi Cai, Kevin Wang, Wuyang Li, Pavlo Molchanov, Peihao Wang, and Zhangyang Wang. Flexgs: Train once, deploy everywhere with many-in-one flexible 3d gaussian splatting. In *Proceedings of the Computer Vision and Pattern Recognition Conference*, 2025.

[6] Radu Beche and Sergiu Nedevschi. Claravid: A holistic scene reconstruction benchmark from aerial perspective with delentropy-based complexity profiling. In *Proceedings of the IEEE/CVF International Conference on Computer Vision*, 2025.

[7] Lu Ling, Yichen Sheng, Zhi Tu, Wentian Zhao, Cheng Xin, Kun Wan, Lantao Yu, Qianyu Guo, Zixun Yu, Yawen Lu, et al. Dl3dv-10k: A large-scale scene dataset for deep learning-based 3d vision. In *Proceedings of the IEEE/CVF Conference on Computer Vision and Pattern Recognition*, 2024.

[8] Shakiba Kheradmand, Daniel Rebain, Gopal Sharma, Weiwei Sun, Yang-Che Tseng, Hossam Isack, Abhishek Kar, Andrea Tagliasacchi, and Kwang Moo Yi. 3d gaussian splatting as markov chain monte carlo. *Advances in Neural Information Processing Systems*, 2024.

[9] Tao Lu, Mulin Yu, Linning Xu, Yuanbo Xiangli, Limin Wang, Dahua Lin, and Bo Dai. Scaffold-gs: Structured 3d gaussians for view-adaptive rendering. In *Proceedings of the IEEE/CVF conference on computer vision and pattern recognition*, 2024.

[10] Michael Niemeyer, Fabian Manhardt, Marie-Julie Rakotosaona, Michael Oechsle, Daniel Duckworth, Rama Gosula, Keisuke Tateno, John Bates, Dominik Kaeser, and Federico Tombari. Radsplat: Radiance field-informed gaussian splatting for robust real-time rendering with 900+ fps. In *2025 International Conference on 3D Vision (3DV)*, 2025.

[11] Saswat Subhajyoti Mallick, Rahul Goel, Bernhard Kerbl, Markus Steinberger, Francisco Vicente Carrasco, and Fernando De La Torre. Taming 3dgs: High-quality radiance fields with limited resources. In *SIGGRAPH Asia 2024 Conference Papers*, 2024.

[12] Guangchi Fang and Bing Wang. Mini-splatting: Representing scenes with a constrained number of gaussians. In *European conference on computer vision*, 2024.

[13] Dmytro Kotovenko, Olga Grebenkova, and Björn Ommer. Edgs: Eliminating densification for efficient convergence of 3dgs. In *Proceedings of the IEEE/CVF Conference on Computer Vision and Pattern Recognition*, 2025.

[14] Panagiotis Papantonakis, Georgios Kopanas, Bernhard Kerbl, Alexandre Lanvin, and George Drettakis. Reducing the memory footprint of 3d gaussian splatting. *Proceedings of the ACM on Computer Graphics and Interactive Techniques*, 2024.

[15] Zhiwen Fan, Kevin Wang, Kairun Wen, Zehao Zhu, Dejia Xu, and Zhangyang Wang. Lightgaussian: Unbounded 3d gaussian compression with 15x reduction and 200+ fps. *Advances in neural information processing systems*, 2024.

[16] Binbin Huang, Zehao Yu, Anpei Chen, Andreas Geiger, and Shenghua Gao. 2d gaussian splatting for geometrically accurate radiance fields. In *ACM SIGGRAPH 2024 conference papers*, 2024.

[17] Jan Held, Renaud Vandeghen, Adrien Deliege, Abdullah Hamdi, Daniel Rebain, Silvio Giancola, Anthony Cioppa, Andrea Vedaldi, Bernard Ghanem, Andrea Tagliasacchi, et al. Triangle splatting for real-time radiance field rendering. In *Thirteenth International Conference on 3D Vision*, 2025.

[18] Jan Held, Renaud Vandeghen, Sanghyun Son, Daniel Rebain, Matheus Gadelha, Yi Zhou, Ming C Lin, Marc Van Droogenbroeck, and Andrea Tagliasacchi. Triangle splatting+: Differentiable rendering with opaque triangles. *arXiv preprint arXiv:2509.25122*, 2025.

[19] Jonathon Luiten, Georgios Kopanas, Bastian Leibe, and Deva Ramanan. Dynamic 3d gaussians: Tracking by persistent dynamic view synthesis. In *3DV*, 2024.

[20] Guanjun Wu, Taoran Yi, Jiemin Fang, Lingxi Xie, Xiaopeng Zhang, Wei Wei, Wenyu Liu, Qi Tian, and Xinggang Wang. 4d gaussian splatting for real-time dynamic scene rendering. In *Proceedings of the IEEE/CVF Conference on Computer Vision and Pattern Recognition (CVPR)*, June 2024.

[21] Yuang Shi, Géraldine Morin, Simone Gasparini, and Wei Tsang Ooi. LapisGS: Layered progressive 3D Gaussian splatting for adaptive streaming. In *Proceedings of the 2025 International Conference on 3D Vision (3DV)*, 2025.

[22] Yuan-Chun Sun, Yuang Shi, Cheng-Tse Lee, Mufeng Zhu, Wei Tsang Ooi, Yao Liu, Chun-Ying Huang, and Cheng-Hsin Hsu. LTS: A DASH streaming system for dynamic multi-layer 3D Gaussian splatting scenes. In *Proceedings of the 16th ACM Multimedia Systems Conference, MMSys 2025, Stellenbosch, South Africa, 31 March 2025 - 4 April 2025*. ACM, 2025.

[23] Antoine Guédon and Vincent Lepetit. Sugar: Surface-aligned gaussian splatting for efficient 3d mesh reconstruction and high-quality mesh rendering. In *Proceedings of the IEEE/CVF conference on computer vision and pattern recognition*, 2024.

[24] Minghan Qin, Wanhua Li, Jiawei Zhou, Haoqian Wang, and Hanspeter Pfister. Langsplat: 3d language gaussian splatting. In *Proceedings of the IEEE/CVF Conference on Computer Vision and Pattern Recognition*, 2024.

[25] Mingqiao Ye, Martin Danelljan, Fisher Yu, and Lei Ke. Gaussian grouping: Segment and edit anything in 3d scenes. In *European conference on computer vision*, 2024.

[26] Hugues Hoppe. Progressive meshes. In *Proceedings of the 23rd annual conference on Computer graphics and interactive techniques*. ACM, 1996.

[27] Kerui Ren, Lihan Jiang, Tao Lu, Mulin Yu, Linning Xu, Zhangkai Ni, and Bo Dai. Octree-gs: Towards consistent real-time rendering with lod-structured 3d gaussians. *IEEE Transactions on Pattern Analysis and Machine Intelligence*, 2025.

[28] Bernhard Kerbl, Andreas Meuleman, Georgios Kopanas, Michael Wimmer, Alexandre Lanvin, and George Drettakis. A hierarchical 3d gaussian representation for real-time rendering of very large datasets. *ACM Transactions On Graphics (TOG)*, 2024.

[29] Yunji Seo, Young Sun Choi, Hyun Seung Son, and Youngjung Uh. Flod: Integrating flexible level of detail into 3d gaussian splatting for customizable rendering. *ACM Transactions on Graphics (Proceedings of SIGGRAPH)*, 2025.

[30] Yang Liu, Chuanchen Luo, Lue Fan, Naiyan Wang, Junran Peng, and Zhaoxiang Zhang. Citygaussian: Real-time high-quality large-scale scene rendering with gaussians. In *European Conference on Computer Vision*, 2024.

[31] Jiaqi Lin, Zhihao Li, Xiao Tang, Jianzhuang Liu, Shiyong Liu, Jiayue Liu, Yangdi Lu, Xiaofei Wu, Songcen Xu, Youliang Yan, et al. Vastgaussian: Vast 3d gaussians for large scene reconstruction. In *Proceedings of the IEEE/CVF Conference on Computer Vision and Pattern Recognition*, 2024.

[32] Jonas Kulhanek, Marie-Julie Rakotosaona, Fabian Manhardt, Christina Tsalicoglou, Michael Niemeyer, Torsten Sattler, Songyou Peng, and Federico Tombari. LODGE: Level-of-detail large-scale Gaussian splatting with efficient rendering. In *Proceedings of the 39th International Conference on Neural Information Processing Systems*, 2025.

[33] Peter Hedman, Julien Philip, True Price, Jan-Michael Frahm, George Drettakis, and Gabriel Brostow. Deep blending for free-viewpoint image-based rendering. *ACM Transactions on Graphics (ToG)*, 2018.

[34] Jonathan T Barron, Ben Mildenhall, Dor Verbin, Pratul P Srinivasan, and Peter Hedman. Mip-nerf 360: Unbounded anti-aliased neural radiance fields. In *Proceedings of the IEEE/CVF conference on computer vision and pattern recognition*, 2022.

[35] Arno Knapitsch, Jaesik Park, Qian-Yi Zhou, and Vladlen Koltun. Tanks and temples: Benchmarking large-scale scene reconstruction. *ACM Transactions on Graphics (ToG)*, 2017.

[36] Zehao Yu, Anpei Chen, Binbin Huang, Torsten Sattler, and Andreas Geiger. Mip-splatting: Alias-free 3d gaussian splatting. In *Proceedings of the IEEE/CVF Conference on Computer Vision and Pattern Recognition (CVPR)*, June 2024.

[37] Barry G Haskell and Arun N Netravali. *Digital pictures: representation, compression, and standards*. Perseus Publishing, 1997.

[38] Zhou Wang, Alan C Bovik, Hamid R Sheikh, and Eero P Simoncelli. Image quality assessment: from error visibility to structural similarity. *IEEE transactions on image processing*, 2004.

[39] Claude Elwood Shannon. A mathematical theory of communication. *The Bell system technical journal*, 1948.

[40] Kieran G Larkin. Reflections on shannon information: In search of a natural information-entropy for images. *arXiv preprint arXiv:1609.01117*, 2016.

[41] Vickie Ye, Ruilong Li, Justin Kerr, Matias Turkulainen, Brent Yi, Zhuoyang Pan, Otto Seiskari, Jianbo Ye, Jeffrey Hu, Matthew Tancik, and Angjoo Kanazawa. gsplat: An open-source library for gaussian splatting. *Journal of Machine Learning Research*, 2025.

[42] Richard Zhang, Phillip Isola, Alexei A Efros, Eli Shechtman, and Oliver Wang. The unreasonable effectiveness of deep features as a perceptual metric. In *Proceedings of the IEEE conference on computer vision and pattern recognition*, 2018.

A Limitations

We identify three limitations that needs discussing of our approach, namely the optimization stability, the nature of our complexity prior, and view conditioning.
(i) Our method inherits the stochastic relocation dynamics of 3DGS-MCMC, so results can slightly vary across runs. This variation does not alter our standing relative to prior work, as our method maintains its relative position at every capacity level and on every dataset we evaluate. The instability is moreover present to the same degree in 3DGS-MCMC and MGS, since all three build on the same relocation mechanism.
(ii) The complexity prior we introduce is computed from the input images alone, and therefore captures spatial difficulty but neither view-dependent appearance nor semantic saliency. A specular highlight that shifts with viewpoint, or a small object that is salient despite low pixel complexity, receives no special treatment under our prior, and the correlations of Tab. 1 should accordingly be read as holding under standard capture conditions.
(iii) Primitive selection is likewise unconditioned on the viewpoint: the formulation is neither distance- nor resolution-dependent, and is thus not designed to suppress aliasing when rendering from distant viewpoints or at reduced resolution. However, its preference for large-support primitives in simple regions may reduce the retention of subpixel primitives relative to opacity-only ranking, but this provides no antialiasing guarantee. Because we modify primitive allocation and ordering without prescribing a competing filtering mechanism, our representation remains compatible in principle with dedicated approaches such as the smoothing filter of Mip-Splatting [36], a combination we do not evaluate here.

B Implementation details

B.1 Pilot Study

Experimental setup. We run the study on the DL3DV [7] test set of 140 scenes, reconstructed with 3DGS-MCMC [8], a robust 3DGS approach. Each scene is labeled bounded or unbounded from the DL3DV metadata and receives 1.0M primitives when bounded and 1.5M when unbounded, reflecting the larger extent of unbounded captures. All scenes are trained at 960p for 30k steps under the default 3DGS-MCMC hyperparameters, holding out every 8th frame as the test split. We measure reconstruction quality with PSNR [37] and SSIM [38], and image complexity with three functionals: Shannon pixel entropy [39, 37], Laplacian response [37], and delentropy [40]. Throughout our study, we exclude the particles that do not contribute to the final reconstruction.

3D aggregation of quality and complexity. The 3D fields Q^{3D} and C^{3D} defined in Eq. 2 of the main paper are constructed by projecting the per-view 2D maps onto the trained Gaussian set under multi-view aggregation. To analyse the joint distribution of complexity, quality, and Gaussian density at the scene level (Fig. 2a), we voxelize each scene using a fixed voxel size of 0.1 in the Colmap normalised scene coordinates. This fixed scale is well defined because DL3DV test scenes are released in a roughly similar normalized frame, so a single voxel size yields comparable spatial granularity across scenes without per-scene tuning. Within each voxel we record (i) the mean local complexity, (ii) the mean reconstruction quality (PSNR or SSIM), and (iii) the number of Gaussians whose means fall inside.

B.2 Method

Scope of the LoD Formulation. Our formulation provides global, view-independent LoD through a single primitive ordering whose prefixes define successive approximations. Unlike camera-dependent selection over a spatial hierarchy, this ordering is fixed across viewpoints and budgets, enabling progressive streaming by transmitting additional primitives as the budget increases.

Complexity maps computation. The complexity maps are computed once per scene, before training, and cached to disk. The computation is implemented in PyTorch and runs on the GPU. Its cost depends on the complexity functional, the patch size, and the image resolution, and ranges from $20\,\mathrm{s}$ to $60\,\mathrm{s}$ per scene on the evaluated datasets. As this is a one time preprocessing step, its overhead is negligible relative to training. We use a fixed receptive field of 32 pixels in all experiments, with

a stride of 4 to 8 depending on the image resolution. This setting yielded consistent complexity statistics across input resolutions ranging from 960p (DL3DV) to approx. 1.6K (MipNerf360).

Implementation. We implement our method on top of the 3DGS-MCMC version from the `gsplat` [41] framework. We adopt delentropy as the complexity functional since it attained the highest average rank in the pilot study (Tab. 1), although our method is agnostic to this choice and admits any complexity functional. On a single NVIDIA H100, reconstructing a typical scene with $\sim$2M primitives completes in 15 minutes. All hyperparameters are listed in Tab. 5.

Training details. We train every scene for 30k steps. Each step renders the training view twice, once at full capacity and once at a budget $\tau \sim \mathcal{U}(0,1)$ sampled anew at every step, so that a single optimization covers the whole LoD spectrum. During the first 500 steps we render at full capacity only, so that the full-capacity solution forms before any prefix is optimized. The total objective averages the two reconstruction terms with the variance term of Eq. 6, and adds the regularizers of 3DGS-MCMC:

$$\mathcal{L} = \tfrac{1}{2}\big(\underbrace{\mathcal{L}_{\text{rec}}(\hat{I}_i^{\text{full}}, I_i)}_{\text{full capacity}} + \underbrace{\mathcal{L}_{\text{rec}}(\hat{I}_i^{\tau}, I_i)}_{\text{budget } \tau} + \underbrace{\lambda_{\text{var}}\,\mathcal{L}_{\text{var}}}_{\text{uniform error}}\big) + \underbrace{\lambda_\alpha\,\bar{\alpha}}_{\text{opacity}} + \underbrace{\lambda_\sigma\,\bar{\sigma}}_{\text{scale}}, \tag{7}$$

where $\mathcal{L}_{\text{rec}}$ is the L1+D-SSIM loss of 3DGS, and $\bar{\alpha}$ and $\bar{\sigma}$ are the mean opacity and mean scale of the primitives, weighted by λ_α and λ_σ (Tab. 5). A newly added or relocated Gaussian has no complexity estimate until a training view observes it. We therefore set its complexity to the minimum, so relocation ranks it by opacity alone until the update of Eq. 3 assigns it a value.

Hyperparameter	**Value**
Spatial-variance loss weight λ_{var}	2.0
Importance-score weight λ	2.0
Complexity EMA rate η	0.8
Training LoD sampling distribution	$\tau \sim \mathcal{U}(0, 100\%)$
Dropout rate on normalized complexity $\tilde{C}$	0.2
Training steps	30000

Table 5: **Hyperparameters used in our method.**

C Experimental evaluation.

C.1 Setup

We follow the evaluation protocol of 3DGS-MCMC [8] and report results on MipNerf360 [34] with 7 scenes, Tanks and Temples [35] with 2 scenes, and Deep Blending (DB) [33] with 2 scenes, together covering a wide range of indoor and outdoor capture conditions. We compare against five baselines spanning the design space of LoD for Gaussian Splatting. Two of them yield a prefix renderable ordering directly comparable to ours: Matryoshka Gaussian Splatting (MGS) [2], our closest competitor, and 3DGS-MCMC [8], which we extend with an opacity based ranking. Other two operate only at restricted points of the LoD spectrum: FlexGS [5], a budget conditioned continuous LoD method, and Octree-GS [27], a discrete LoD method. The last, LightGaussian [15], is a pruning method, included to compare our ordering against post hoc decimation at equal capacity. A detailed description of each baseline and its adaptation to our protocol is provided in Sec. C.2. All models are trained under identical conditions on NVIDIA H100 GPUs. For fair comparison we fix the total primitive budget across 3DGS-MCMC, MGS, and our method, while FlexGS and Octree-GS are reported at their native counts. We report PSNR [37], SSIM [38], and LPIPS [42], which capture the complementary axes of pixel fidelity, structural preservation, and perceptual similarity.

C.2 Baselines

3DGS-MCMC [8]. We use the `gsplat` reimplementation with default hyperparameters. Since 3DGS-MCMC is neither LOD-aware at training time nor designed to support budget-conditioned inference, we evaluate it under LOD by applying the simplest possible reduction strategy: at each target budget we retain the top-k primitives ranked by opacity and discard the rest. This naive

trimming establishes the baseline behaviour of an opacity-only ranking signal absent any LOD-aware training.

Matryoshka-GS [2]. We use the authors original implementation. One important difference from their reported setup affects direct comparability: the original paper trains all scenes with a flat 5M-primitive budget for 50k steps. To align with our protocol and with the 3DGS-MCMC budget convention, we instead train MGS for 30k steps and adapt the primitive budget per scene to match the 3DGS allocation. All other hyperparameters follow the original implementation. Notably by doing, we observed that the stability has improved over the DB dataset over the official results.

FlexGS [5]. We use the authors' original implementation and training hyperparameters without modification. FlexGS is a budget-conditioned continuous-LOD method that learns a differentiable selector mapping each primitive to a retention score for a target budget, trained in two stages: a first stage optimises the 3DGS representation, and a second stage trains the selector on top of the frozen primitives. This design trades global consistency for pointwise quality: FlexGS can outperform prefix-ranked methods at the specific budgets it is optimised for, but at the cost of (i) roughly doubled end-to-end training time, and (ii) the absence of a prefix-renderable ordering, since changing the operating LOD requires a fresh forward pass through the selector to recompute per-primitive scores rather than truncating a precomputed ranking.

Octree-GS [27]. We use the authors' original implementation and training hyperparameters without modification. Octree-GS is a discrete-LOD method that organises primitives into a fixed octree hierarchy, exposing a small number of predefined operating points corresponding to traversal depths. This design yields stable quality at its native levels but cannot interpolate between them: budgets falling between two depths are unreachable, and the coarsest level is bounded below by the structure of the hierarchy itself.

LightGaussian [15]. We use the authors' original implementation. LightGaussian is a compression method rather than an LoD one, pruning primitives by a global volumetric importance measure, fine tuning the survivors, then compacting them through spherical harmonic distillation and vector quantisation. We retain only the pruning stage, as the others reduce storage without changing the primitive count that defines our budget axis. For fairness we initialise from the same 30k step 3DGS-MCMC checkpoints as the other baselines so every method starts from an identical primitive set. We omit the recovery fine tuning, since fine tuning at each budget yields a separate optimisation run and a stored model per operating point, which is what separates pruning from a single prefix renderable ordering.

D Additional experiments

In all tables, best results are in **bold** and second best are underlined.

D.1 Additional qualitative results

We complement Fig. 3 with two more MipNerf360 dataset [34] scenes, the outdoor Garden (Fig. 7) and the indoor Room (Fig. 8). Each row shows one budget and each column one method. Insets report the FPS measured over the entire scene and the PSNR of the presented image.

D.2 Dropout ablation

In this section, we investigate how the complexity dropout rate δ used during relocation (Eq. 4) affects reconstruction quality. With this dropout, the complexity term $\tilde{C}_j$ of a candidate g_j is set to zero with probability δ, in which case g_j is not removed from the candidate set but competes for relocation based only on its opacity. The rate δ therefore interpolates between two extremes: at $\delta = 0$, the complexity term is always applied and the relocation weights are fully determined by the complexity field, while at $\delta = 1$, the complexity term is always dropped and the rule reduces to the original opacity sampling $p(g_j) = \alpha_j$. We perform a value sweep $\delta \in \{0, 0.2, 0.4, 0.6, 0.8, 1\}$ on the outdoor Tanks and Temples [35] and the indoor Deep Blending [33] datasets, and report the metrics at full capacity and the AUC over $[0.1\%, 100\%]$ (Tab. 6). Our default value $\delta = 0.2$ attains the best result on all twelve entries, tied with $\delta = 0.4$ only for SSIM at full capacity on Deep Blending. Compared to the original opacity sampling ($\delta = 1$), it improves the AUC PSNR by 0.14 dB on TandT (24.02 vs. 23.88) and by 0.23 dB on Deep Blending (29.51 vs. 29.28). Applying the complexity term at



Figure 7: **Qualitative comparison on Garden.** Renders of the outdoor Garden scene from MipNerf360 [34] at four budgets.

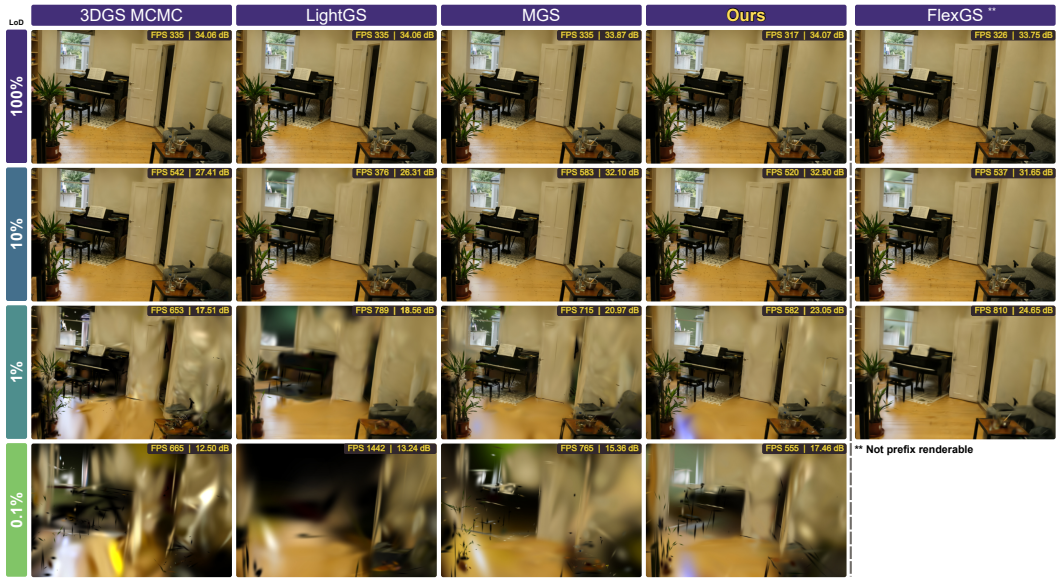


Figure 8: **Qualitative comparison on Room.** Renders of the indoor Room scene from MipNerf360 [34] at four budgets.

every step ($\delta = 0$) is not beneficial either, as it falls below opacity sampling on Deep Blending (29.00 vs. 29.28 AUC PSNR). We hypothesize that without dropout, relocation repeatedly targets the same high complexity regions, whereas occasionally dropping the complexity term lets opacity sampling reach the remaining regions. Large intermediate rates ($\delta \in \{0.6, 0.8\}$) perform worst on both datasets. Although the differences are small relative to the noise of the metrics, the consistency of $\delta = 0.2$ across both datasets supports it as a robust default. We also observe more stable training with complexity dropout, especially on the indoor scenes of Deep Blending.

Dataset	δ	100% Capacity			AUC [0.1%, 100%]		
		PSNR ↑	SSIM ↑	LPIPS ↓	PSNR ↑	SSIM ↑	LPIPS ↓
TandT [35]	0	24.52	0.856	0.153	23.91	0.829	0.193
	0.2	**24.65**	**0.868**	**0.150**	**24.02**	**0.839**	**0.189**
	0.4	24.46	0.852	0.152	23.86	0.828	0.192
	0.6	24.44	0.847	0.163	23.85	0.818	0.195
	0.8	24.39	0.841	0.171	23.80	0.811	0.199
	1	24.45	0.865	0.151	23.88	0.837	0.190
DB [33]	0	29.39	0.905	0.246	29.00	0.896	0.263
	0.2	**29.92**	**0.911**	**0.240**	**29.51**	**0.902**	**0.254**
	0.4	29.63	**0.911**	0.241	29.23	0.900	0.264
	0.6	29.21	0.909	0.252	28.94	0.882	0.269
	0.8	29.19	0.899	0.253	28.90	0.885	0.271
	1	29.75	0.903	0.247	29.28	0.899	0.263

Table 6: **Complexity dropout rate.** Sweep of the dropout rate δ on TandT and DB. $\delta = 0$ always applies the complexity term and $\delta = 1$ reduces to opacity sampling. Our default is shaded.

Method	Indoor				Outdoor			
	100%	10%	1%	0.1%	100%	10%	1%	0.1%
FlexGS* [5]	339	578	833	–	351	609	1021	–
LightGaussian [15]	300	379	697	**1101**	189	435	855	**1364**
3DGS MCMC [8]	300	568	688	732	189	**805**	**1093**	1177
MGS [2]	**302**	**595**	**731**	829	193	769	1050	1151
Ours	**302**	450	475	463	**198**	649	833	874

*FlexGS operates with a smaller primitive budget, hence the faster rendering speed.

Table 7: **Rendering speed.** Average frame rate (FPS ↑) on MipNerf360 at four levels of detail. Indoor scenes are rendered at half resolution and outdoor scenes at quarter resolution. FlexGS is excluded from the ranking.

D.3 Rendering Speed

We investigate the rendering speed of our method against the baselines at four levels of detail (100%, 10%, 1%, 0.1%). We split MipNeRF360 [34] into indoor scenes (Bonsai, Counter, Kitchen, Room) and outdoor scenes (Bicycle, Garden, Stump) and report the average frame rate on a single NVIDIA H100 (Tab. 7). All prefix methods share an identical budget, so their primitive counts match at every level of detail and speed differences stem only from the size of the retained primitives, whereas FlexGS [5] operates with a smaller budget and is not directly comparable. At full capacity, our method is the fastest prefix method, tied with MGS indoors (302 FPS) and ahead outdoors (198 vs. 193 FPS). As the budget shrinks, every method accelerates, but ours does so less and saturates below 1%, reaching 463 FPS indoors and 874 FPS outdoors at 0.1%, against 829 and 1,151 FPS for MGS. We attribute this to our importance score (Eq. 5), which retains large primitives so that simple regions remain covered. A large primitive spans more tiles and thus costs more per frame, whereas MGS favors compact, high opacity primitives that render faster but cover less of the scene, at lower quality (Fig. 4). Our method is thus slower than MGS at low budgets, a cost we accept in exchange for coverage and better quality, while at equal quality it requires fewer primitives (Fig. 6). Reducing the per frame cost of large primitives at the lowest budgets, for instance by bounding their screen footprint, is a natural direction for future work.

D.4 Degradation Across Complexity Levels

In this section, we investigate whether the importance score (Eq. 5) undoes the capacity that complexity guided densification (Eq. 4) adds to complex regions. Since the score reduces to opacity in complex regions, primitives there are ranked with less spatial support and are therefore discarded earlier as the budget shrinks. To quantify this effect, we project the image complexity maps onto the Gaussians with the same aggregation as in our pilot study (Sec. 3), group the Gaussians into five complexity bins, and compare our method with MGS [2] through three statistics per bin as follows. (i) *Allocation*: the number of Gaussians in each bin at full capacity, which shows where densification places the primitives (Tab. 8). (ii) *Survival rate*: for each bin, the percentage of its full capacity

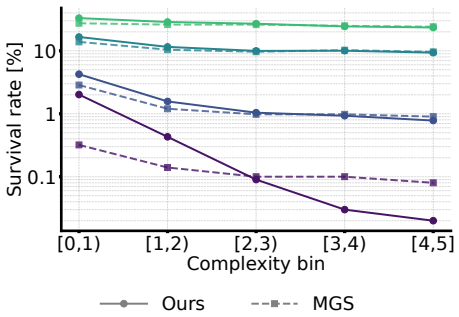


Figure 9: **Survival rate.** Percentage of the Gaussians of each complexity bin at full capacity that are still retained at a given budget (log scale). Our method keeps more Gaussians in simple bins and fewer in complex bins than MGS.

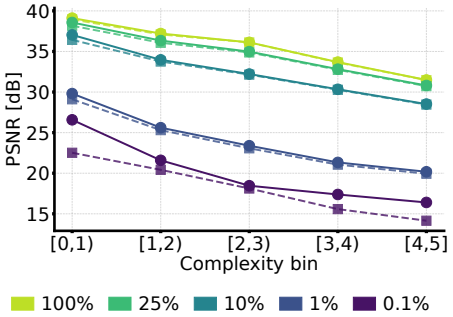


Figure 10: **Quality.** Average PSNR of the Gaussians in each complexity bin, computed from the per pixel error maps projected onto the Gaussians. Our method has the largest gains at the lowest capacity.

Method	**Statistic**	$[0,1)$	$[1,2)$	$[2,3)$	$[3,4)$	$[4,5]$
MGS [2]	Count	22.9k	110.0k	240.1k	466.5k	460.5k
	Share	1.8%	8.5%	18.5%	35.8%	35.4%
Ours	Count	21.1k	100.7k	233.8k	471.5k	472.9k
	Share	1.6%	7.7%	18.0%	36.3%	36.4%

Table 8: **Full capacity allocation.** Number and share of Gaussians per complexity bin at a budget of 1300k. Our densification shifts Gaussians towards the most complex bins.

Gaussians that are still present at a given budget, *i.e.*, a survival rate of 10% means that one in ten Gaussians of that bin is kept (Fig. 9). (iii) *Quality*: we project the per pixel error maps onto the Gaussians with the same aggregation and report the average error of each bin as PSNR (Fig. 10). At full capacity, densification shifts the population towards complex regions, with 472.9k Gaussians in the most complex bin $[4,5]$ against 460.5k for MGS, and 21.1k against 22.9k in the simplest bin $[0,1)$. As the budget shrinks, survival drops with complexity, as intended by the score: at 25% budget, our method retains 33.08% of the Gaussians in $[0,1)$ against 23.47% in $[4,5]$, and at 0.1% the ratio grows to 2.02% against 0.02%. In complex bins, our method thus keeps fewer Gaussians than MGS at low budgets (0.02% vs. 0.08% in $[4,5]$ at 0.1%). This reduced survival does not translate into lower quality, as our method attains a higher PSNR than MGS in every bin and at every budget, including the most complex bin, where the gap grows from $+0.02$ dB at 100% to $+2.25$ dB at 0.1% (16.40 vs. 14.15). These results suggest that the Gaussians retained in complex regions are better placed by densification, so that the capacity removed by the score is compensated rather than reintroduced as a failure mode.

D.5 Extended ablation

We complement the aggregate results of Sec. 5.4 with a breakdown at individual LoD budgets on MipNeRF360. Table 9 reports all component combinations at 100%, 10%, 1%, and 0.1% capacity, alongside the AUC values reported in the main paper. Among the individual components, importance scoring produces the strongest improvements across all three metrics at every reduced budget, increasing PSNR at 0.1% from 14.59 to 15.94 dB. Densification also improves low-budget quality, reaching 15.68 dB at 0.1%, while the variance loss alone provides smaller gains. Combining densification and scoring further raises PSNR to 16.08 dB at this budget, and adding the variance loss brings it to 16.18 dB. The complete method achieves the best results across all metrics and evaluated budgets. Its PSNR gain over the baseline increases from 0.25 dB at full capacity to 0.80, 0.93, and 1.59 dB at 10%, 1%, and 0.1%, respectively, showing that the improvements are most pronounced under aggressive budget reduction.

	Components			AUC [0.1%, 100%]			100% Capacity			10% Capacity			1% Capacity			0.1% Capacity		
	Dens.	Score	Var.	PSNR ↑	SSIM ↑	LPIPS ↓	PSNR ↑	SSIM ↑	LPIPS ↓	PSNR ↑	SSIM ↑	LPIPS ↓	PSNR ↑	SSIM ↑	LPIPS ↓	PSNR ↑	SSIM ↑	LPIPS ↓
None	✗	✗	✗	28.74	0.855	0.196	29.55	0.863	0.164	27.02	0.794	0.275	20.12	0.543	0.540	14.59	0.393	0.623
Single	✓	✗	✗	28.81	0.859	0.190	29.79	0.889	0.151	27.53	0.805	0.263	20.76	0.560	0.511	15.68	0.424	0.616
	✗	✓	✗	28.94	0.861	0.188	29.62	0.882	0.159	27.69	0.818	0.259	20.95	0.564	0.511	15.94	0.457	0.615
	✗	✗	✓	28.79	0.855	0.190	29.59	0.870	0.160	27.44	0.804	0.268	20.39	0.553	0.520	15.10	0.412	0.621
Pair	✓	✓	✗	28.99	0.862	0.187	29.75	0.885	0.154	27.75	0.819	0.259	20.99	0.565	0.510	16.08	0.457	0.615
	✓	✗	✓	28.75	0.850	0.197	29.70	0.877	0.159	27.61	0.812	0.262	20.70	0.556	0.514	15.22	0.415	0.620
	✗	✓	✓	28.95	0.860	0.189	29.71	0.880	0.155	27.74	0.816	0.260	20.77	0.559	0.512	15.96	0.456	0.615
All	✓	✓	✓	**29.09**	**0.867**	**0.184**	**29.80**	**0.893**	**0.150**	**27.82**	**0.822**	**0.257**	**21.05**	**0.566**	**0.508**	**16.18**	**0.458**	**0.612**

Table 9: **Full ablation.** All combinations of complexity aware densification (Dens.), importance scoring (Score), and the spatial variance loss (Var.) on MipNeRF360.

LoD	**MGS**[2] # holes ↓	**Ours** # holes ↓
100%	0	0
10%	0	0
1%	2,615	**2,420**
0.1%	83,341	**20,765**

(a) Bonsai

LoD	**MGS**[2] # holes ↓	**Ours** # holes ↓
100%	0	0
10%	0	0
1%	11,884	**2,204**
0.1%	116,920	**36,009**

(b) Bicycle

Table 10: **Coverage across LoDs.** Number of "hole" pixels, *i.e.*, pixels whose accumulated opacity is below 0.05, on the test set of the indoor Bonsai and outdoor Bicycle scenes[34]. Lower is better.

D.6 Coverage Across LoDs

In this experiment, we investigate whether the primitives retained at low budgets still cover the whole scene. A reduced budget can degrade a rendering in two ways: the scene may be represented at a coarser resolution, or parts of it may no longer be covered by any primitive, leaving "holes". We further define such holes as a pixel whose accumulated opacity is $\alpha < 0.05$ and count such pixels over all test views at 4 LoDs (100, 10, 1, 0.1). We compare against MGS [2], our closest prefix renderable competitor, on two MipNerf360 scenes [34]: the indoor Bonsai and the outdoor Bicycle. Tab. 10 shows that coverage is preserved by both methods at high budgets and that the differences emerge as the budget shrinks. At 100% and 10% capacity, neither method leaves any hole. At 1% capacity, the two methods are close on Bonsai ($2{,}420$ vs. $2{,}615$ hole pixels), whereas on Bicycle MGS already leaves $5.4\times$ more holes than ours ($11{,}884$ vs. $2{,}204$). At 0.1% capacity, our method leaves fewer holes on both scenes, with MGS producing $4.0\times$ more on Bonsai ($83{,}341$ vs. $20{,}765$) and $3.2\times$ more on Bicycle ($116{,}920$ vs. $36{,}009$). We attribute this difference to our importance score (Eq. 5), which retains large primitives in simple regions, so that areas such as the background remain covered by a few large Gaussians as the budget shrinks. The same mechanism explains why the gap appears earlier on Bicycle, whose large and simple outdoor background is the first to be removed by an ordering that does not account for coverage.

E Inter and Intra LOD Variance Measure

We formally define here the inter and intra LoD variance measurement. Let $\Delta_t^m(p)$ denote the direction-corrected quality degradation of patch p between two consecutive LoDs $\tau_t \to \tau_{t+1}$, the inter LoD variance writes:

$$V_{\text{inter}}^m = \frac{1}{|\mathcal{P}|} \sum_{p \in \mathcal{P}} \text{Var}_t[\Delta_t^m(p)] \ , \tag{8}$$

which measures whether the same patch degrades smoothly across consecutive LoD transitions. Similarly, the intra LoD variance measurement writes:

$$V_{\text{intra}}^m = \frac{1}{T-1} \sum_{t=1}^{T-1} \text{Var}_{p \in \mathcal{P}}[\Delta_t^m(p)] \ , \tag{9}$$

and measures whether one LoD transition degrades the image uniformly across patches.